ARTICLE

Chinese Journal of Structural Chemistry

In-situ Construction of Sulfur-doped g-C_3N_4/defective g-C_3N_4 Isotype Step-scheme Heterojunction for Boosting Photocatalytic H_2 Evolution

Jing Zou[1], Guodong Liao[1], Jizhou Jiang[1,2]*, Zhiguo Xiong[1], Saishuai Bai[1], Haitao Wang[1]*, Pingxiu Wu[3], Peng Zhang[4] and Xin Li[5]*

[1]*School of Environmental Ecology and Biological Engineering, School of Chemistry and Environmental Engineering, Key Laboratory of Green Chemical Engineering Process of Ministry of Education, Engineering Research Center of Phosphorus Resources Development and Utilization of Ministry of Education, Wuhan Institute of Technology, Wuhan 430205, China*

[2]*Key Laboratory of Rare Mineral, Ministry of Natural Resources, Geological Experimental Testing Center of Hubei Province, Wuhan 430034, China*

[3]*Semiconductor Electronic Special Gas of Hubei Engineering Research Center, Jingzhou, Hubei 434000, China*

[4]*State Center for International Cooperation on Designer Low-Carbon & Environmental Materials (CDLCEM), School of Materials Science and Engineering, Zhengzhou University, Zhengzhou 450001, China*

[5]*Institute of Biomass Engineering, Key Laboratory of Energy Plants Resource and Utilization, Ministry of Agriculture and Rural Affairs, South China Agricultural University, Guangzhou 510642, China*

ABSTRACT The rational construction of a high-efficiency step-scheme heterojunctions is an effective strategy to accelerate the photocatalytic H_2. Unfortunately, the variant energy-level matching between two different semiconductor confers limited the photocatalytic performance. Herein, a newfangled graphitic-carbon nitride (g-C_3N_4) based isotype step-scheme heterojunction, which consists of sulfur-doped and defective active sites in one microstructural unit, is successfully developed by in-situ polymerizing N,N-dimethylformamide (DMF) and urea, accompanied by sulfur (S) powder. Therein, the polymerization between the amino groups of DMF and the amide group of urea endows the formation of rich defects. The propulsive integration of S-dopants contributes to the excellent fluffiness and dispersibility of lamellar g-C_3N_4. Moreover, the developed heterojunction exhibits a significantly enlarged surface area, thus leading to the more exposed catalytically active sites. Most importantly, the simultaneous introduction of S-doping and defects in the units of g-C_3N_4 also results in a significant improvement in the separation, transfer and recombination efficiency of photo-excited electron-hole pairs. Therefore, the resulting isotype step-scheme heterojunction possesses a superior photocatalytic H_2 evolution activity in comparison with pristine g-C_3N_4. The newly afforded metal-free isotype step-scheme heterojunction in this work will supply a new insight into coupling strategies of heteroatoms doping and defect engineering for various photocatalytic systems.

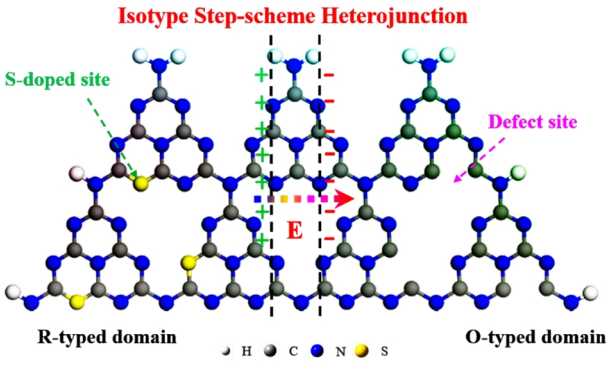

Keywords: sulfur-doping, defects, isotype step-scheme heterojunction, g-C_3N_4, photocatalytic H_2

n INTRODUNTION

Photocatalytic splitting of water to generate H_2 is one of the most promising technologies to the mitigation of environmental pollution and energy crisis caused by the widespread employ of fossil energy.[1–3] However, the sluggish kinetics of hydrogen evolution reactions severely affects the scale application of water splitting.[4–6] Consequently, intensive efforts have been devoted to exploring efficient, robust and economical photocatalysts in the past few decades, including non-noble metal-based composite, ultra-low precious metal supported compounds and non-metallic materials.[7–12] Thereinto, graphitic-carbon nitride (g-C_3N_4) as the representation of metal-free catalysts is considered proverbially as a charming material for photocatalytic H_2 evolution due to the inherent advantages of economic fabrication, excellent visible light response, specific two-dimensional layered structure, and suitable band gap, as well as the high chemical and thermal stability.[9,13–15] Nevertheless, the limited redox potential, fast photo-excited carrier recombination rate, poor visible light absorption and small photocatalytic surface active sites tremendously impede the photocatalytic H_2 evolution properties of pristine g-C_3N_4.[16,17]

In this respect, various modification strategies have been devoted to consolidating the photocatalytic H_2 evolution performance of pristine g-C_3N_4, such as coupling with other semiconductors to form miscellaneous heterojunctions, structural optimizing to increase surface area and active sites density, and metal or non-metal doping to capture photo-generated electrons or holes.[18–21] Therein, the most effective strategy is to construct an intimate heterojunction between g-C_3N_4 and another semiconductor, which is conducive to the inhibited recombination rate of photo-excited carriers through the spatial separation of electrons and holes.[22–24] Representatively, step-scheme heterojunctions as a new-fashioned direct Z-scheme structure exhibit extraordinary superiorities.[25,26] A typical step-scheme heterojunction is invariably composed of two n-type semiconductors with

DOI: 10.14102/j.cnki.0254-5861.2021-0039

staggered band configurations, of which one is considered to be of the oxidation photocatalyst, while the other is assigned to the reduction photocatalyst.[17,27,28] The widely divergent redox capacity between the two materials endows the formation of internal electric field at the interface of two n-type semiconductors, thereby offering an internal driving force to boost the transfer efficiency of photo-excited carriers.[29,30] Therefore, the high-reductive electrons are enriched in the valence band of reduced semiconductor to induce the reduction of hydrogen ions (H^+), thus obtaining the superior photocatalytic H_2 evolution activity.[31,32] Accordingly, numerous g-C_3N_4 relevant step-scheme heterojunctions have been developed as high-efficient H_2 evolution photocatalysts, such as N-doped MoS_2/S-doped g-C_3N_4,[33] $W_{18}O_{49}$/porous g-C_3N_4,[34] WO_3/g-C_3N_4,[35] Co_3S_4/g-C_3N_4,[31] TiO_2/g-C_3N_4,[36] $Cd_{0.5}Zn_{0.5}S$/g-C_3N_4[37] and WO_3/WS_2/g-C_3N_4.[38] However, the variant energy level matching between two different semiconductors still confers limited photocatalytic performance. Moreover, the current synthetic strategies are time-consuming and quite tedious, which commonly involve the separate preparation of two n-type semiconductors and then recombination to form a heterojunction. Therefore, the exploration of a neoteric isotype S-scheme heterojunction with similar electronic band structure and lattice matching *via* a simple and convenient methodology is highly desirable, but remains challenging. Additionally, the introduction of defects, especially surface defects, can significantly regulate the electronic and optical properties of semiconductors.[39,40] Believably, the combination of defect-engineered g-C_3N_4 may remarkably enhance the photoelectrochemical performances and interfacial carrier transfer efficiency of g-C_3N_4 based step-scheme heterostructures.[41,42] Nevertheless, the introduction of defect-engineering into S-scheme heterojunctions for photocatalytic H_2 evolution has been scarcely reported so far.

In this context, a novel defect-engineered isotype step-scheme heterojunction, accompanied by sulfur-doping and defect active sits in the same microstructural unit of g-C_3N_4, is developed as an advanced H_2 evolution photocatalyst for the first time *via* in-situ thermal polymerizing N,N-dimethylformamide (DMF) and urea in the presence of sulfur powder. Particularly, the simultaneous integration of S-dopants and abundant defects endows the excellent fluffiness and dispersibility of lamellar g-C_3N_4, thereby exposing rich active embedding sites. Moreover, the coupling of isotype step-scheme heterojunctions between sulfur-dopants and affluent defects can not only enhance the transfer and separation efficiency, but also improve the absorption of photons and the lifetime of photo-generated electron-hole pairs. Consequently, the optimal photocatalyst possesses outstanding photocatalytic H_2 evolution activity in terms of the H_2 generation rate of 3110.1 $\mu mol \cdot g^{-1} \cdot h^{-1}$, which is around 9 times higher than that of pristine g-C_3N_4 (373.6 $\mu mol \cdot g^{-1} \cdot h^{-1}$). Furthermore, the mechanism of the enhanced photocatalytic performance of g-C_3N_4 by constructing a defect-engineered isotype step-scheme heterojunction is also in deep investigation.

n RESULTS AND DISCUSSION

The meticulous preparation process of sulfur-doped defect-rich graphitic-carbon nitride (S-g-C_3N_4-D) is illustrated in Figure 1a. Normally, a well-known high-temperature polymerization reaction takes place between the amide groups of three urea molecules to construct the geometric g-C_3N_4 monomer.[43] Discriminatively,

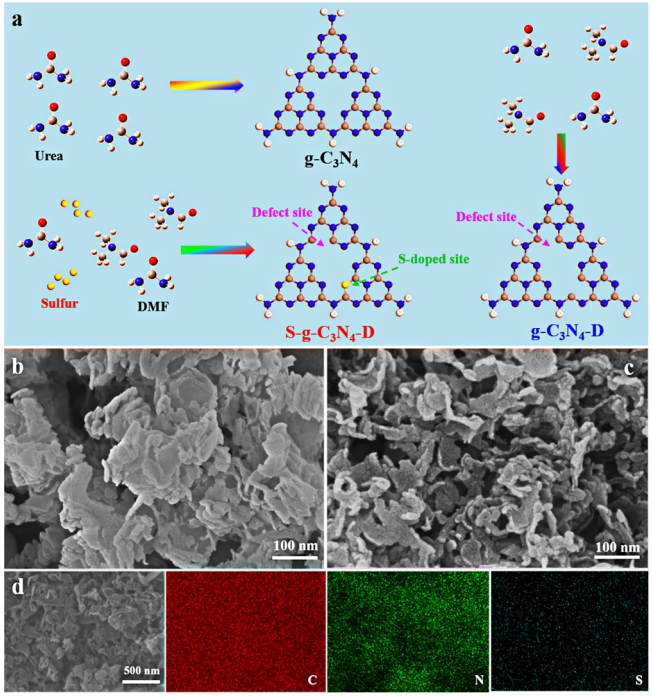

Figure 1. (a) Schematic illustration for the fabrication of g-C_3N_4, g-C_3N_4-D and S-g-C_3N_4-D. (b) FESEM image of g-C_3N_4-D. (c) FESEM image of S-g-C_3N_4-D and (d) Corresponding EDX elemental mapping images of C, N and S.

after the introduction of DMF molecules, the amide group of the urea molecule and one of the amino groups of DMF undergo polycondensation to remove one water molecule, which terminates further reactions with other urea molecules, thus creating a defective site in the monomer of g-C_3N_4. Meanwhile, a few sulfur atoms produced by the sublimation of sulfur powder are intercalated smoothly into the defect sites, resulting in the in-situ formation of sulfur-doped g-C_3N_4 with abundant defects.

The typical scanning electron microscopy (SEM) image of Figure S1 indicates that the obtained g-C_3N_4 possesses a well-defined lamellar morphology. The SEM observation of Figure 1b suggests that the g-C_3N_4-D formed by the introduction of DMF still maintains the flake-like nanostructure, revealing the occurred polymerization between urea and DMF molecules (Figure 1a). Figure 1c exhibits the SEM image of S-g-C_3N_4-D, where the smaller size and thinner sheets are observed in comparison with that of g-C_3N_4 and g-C_3N_4-D, revealing the good fluffiness and dispersibility of S-g-C_3N_4-D due to the introduction of defects and sulfur doping. The detail microstructures of abstained samples are further evaluated by transmission electron microscopy technique (TEM). The TEM observation in Figure S2 and S3 suggest that the definitive lamellar nanoframework is completely preserved after the integration of DMF and sulfur powder. To investigate the element composition and distribution of S-g-C_3N_4-D, Energy dispersive X-ray spectroscopy (EDX) measurement is carried out firstly. Figure 1d presents the element mappings of C, N and S for the S-g-C_3N_4-D sample, in which the obvious and homogeneous S element signal confirms the successful doping and uniform distribution of sulfur species.

X-ray diffraction (XRD) patterns of developed photocatalysts are investigated to study the structural defects and crystal types.

DOI: 10.14102/j.cnki.0254-5861.2021-0039

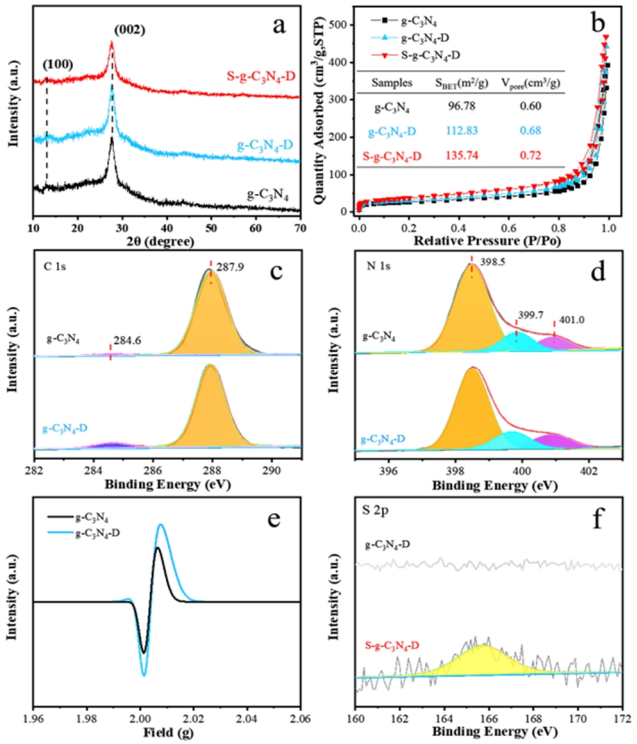

Figure 2. (a) XRD patterns and (b) corresponding N_2 sorption isotherms of g-C_3N_4, g-C_3N_4-D and S-g-C_3N_4-D. (c) High-resolution XPS spectra of C 1*s* and (d) N 1*s* for g-C_3N_4 and g-C_3N_4-D. (e) EPR spectra of g-C_3N_4 and g-C_3N_4-D. (f) High-resolution XPS spectra of S 2*p* for g-C_3N_4-D and S-g-C_3N_4-D.

Figure 2a exhibits the XRD patterns of g-C_3N_4, g-C_3N_4-D and S-g-C_3N_4-D, where the two obvious diffraction peaks located at approximately 13.1° and 27.2° correspond well to the (100) and (002) diffraction planes of g-C_3N_4. Therein, the (100) plane represents the in-plane structure stacking pattern, while the (002) crystal reflection relates to the inter-planar stacking of conjugated aromatic units.[44] The similar XRD spectra of g-C_3N_4-D and S-g-C_3N_4-D compared with that of g-C_3N_4 demonstrate the unchanging phase of g-C_3N_4 even with the addition of DMF and sulfur powder in the synthesis process. Notably, the S-g-C_3N_4-D exhibits a broader FWHM with a weaker intensity compared to that of g-C_3N_4-D, further confirming that sulfur doping effectively strips bulk g-C_3N_4 into thin nanosheets by overcoming weak van der Waals forces between adjacent heptazine layers of g-C_3N_4,[45] which is consistent with the results of SEM (Figure 1b and 1c). Additionally, the almost disappeared (100) diffraction plane of g-C_3N_4-D in comparison to that of g-C_3N_4 reveals that the polymerization between DMF and urea molecules increases the number of defects into the in-planes of the structural unit of g-C_3N_4,[46] thereby reducing the orderliness of microcosmic framework (Figure 1a). To disclose the porosity textural features and specific surface areas of explored g-C_3N_4, g-C_3N_4-D and S-g-C_3N_4-D catalysts, the nitrogen adsorption-desorption isotherms and the corresponding Barrette-Joynere-Halenda (BJH) pore size distributions are analyzed, as presented in Figure 2b and S4. The type II isotherms with a typical H_4 hysteresis loop suggest the coexistence of micropores and mesopores in g-C_3N_4, g-C_3N_4-D and S-g-C_3N_4-D materials.[47] Moreover, the BET surface area of S-g-C_3N_4-D is 135.74 $m^2 \cdot g^{-1}$ (Table S1), which is much higher than that of g-C_3N_4 (96.78 $m^2 \cdot g^{-1}$) and g-C_3N_4-D (112.83 $m^2 \cdot g^{-1}$), indicating excellent dispersibility and fluffiness of S-g-C_3N_4-D again. Noteworthy, the S-g-C_3N_4-D possesses the highest surface area (135.74 $m^2 \cdot g^{-1}$), biggest average pore size (2.58 nm) and largest total pore volume (0.72 $cm^3 \cdot g^{-1}$) among all developed photocatalysts, which not only contribute to expose abundant photocatalytic active surface sites, but also conduce to enhance the migration rate of photo-excited carriers, thus anticipating to the excellent photocatalytic activity.[48]

The surface elemental compositions and bonding configurations of S-g-C_3N_4-D are further examined by X-ray photoelectron spectroscopy (XPS) analysis. The full XPS survey of S-g-C_3N_4-D sample (Figure S5) demonstrates the presence of C, N and S elements, and the corresponding elemental surface contents are found to be 42.13 at%, 57.70 at% and 0.17 at%. Worth mentioning, only a small number of S atoms are inserted into the defect sites of g-C_3N_4 structural monomer, thus forming a unique microstructure in which S-doping and defect sites coexist. To accurate probe the bonding configurations of developed photocatalysts, the corresponding high-resolution XPS spectra of C 1*s*, N 1*s* and S 2*p* are investigated detailedly. Figure 2c and S6a exhibit the high-resolution C 1*s* spectra of g-C_3N_4, g-C_3N_4-D and S-g-C_3N_4-D, in which the peak observed at 284.6 eV belongs to the C–C bond, while another one at 287.9 eV corresponds well to the N–C=N bond.[49–51] Therein, the peak area percentage of N–C=N bond (287.9 eV) decreases obviously from 98.3% for g-C_3N_4 to 93.3% for g-C_3N_4-D (Table S2), revealing the formation of defects as displayed in Figure 1a. Meanwhile, the corresponding high-resolution N 1*s* spectra can be deconvoluted into three distinct peaks centered at 398.5, 399.7 and 401.0 eV (Figure 2d and S6b), which allocate well to the three nitrogen bonds of N–C=N, N–$(C)_3$ and -NH in the structural unit of g-C_3N_4, respectively.[52,53] As expected, the peak area percentage of N–C=N bond (398.5 eV) reduces to 70.1% for the g-C_3N_4-D sample, which is obviously smaller than that of g-C_3N_4 (74.7%, Table S2), suggesting the successful integration of defects into g-C_3N_4 again. Moreover, the electron paramagnetic resonance (EPR) spectra of g-C_3N_4 and g-C_3N_4-D materials are recorded to further identify the structural differences before and after the introduction of defects. As illustrated in Figure 2e, the g-C_3N_4-D sample possesses the stronger peak intensity in comparison to that of g-C_3N_4, which indicates that the DMF-assisted thermal polymerization can introduce more defects into g-C_3N_4 clearly, thus forming more unsaturated photocatalytic active sites. Figure 3f depicts the high-resolution S 2*p* spectra of g-C_3N_4-D and S-g-C_3N_4-D samples, where the strong peaks observed at 165.4 eV confirm the presence of C–S–C bond,[54] convincingly proofing the successful insertion of S atom into the carbon skeleton of g-C_3N_4.

Motivated by characteristic S doped and rich-defect g-C_3N_4 nanoframework, large specific surface area nanoskeleton and excellent photons absorption ability, the photocatalytic activities of developed catalysts are investigated by testing the H_2 evolution efficiency for water splitting under visible light irradiation. Before that, the additive amounts of DMF and powdered sulfur in the synthesis process are optimized firstly. Notably, the differences of photocatalytic H_2 evolution activities observed in Figure 3a and 3b suggest that the optimal addition of DMF and the most

DOI: 10.14102/j.cnki.0254-5861.2021-0039

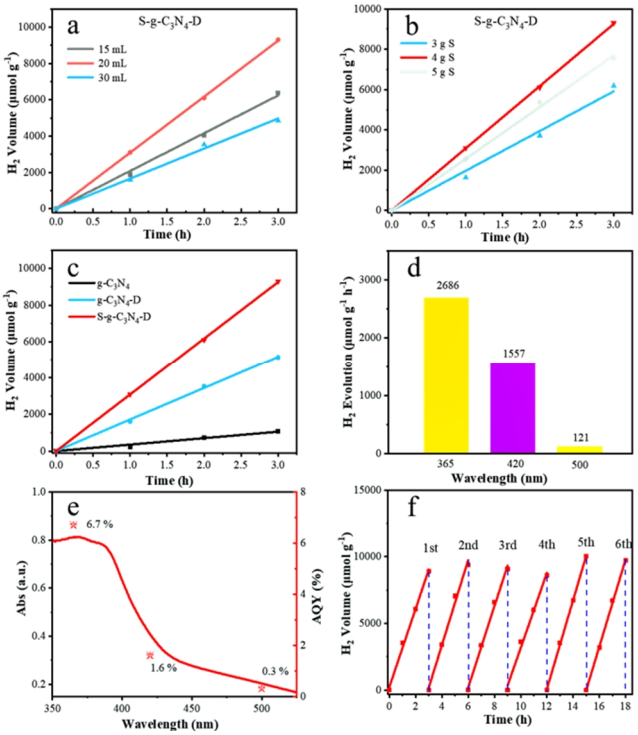

Figure 3. (a) Photocatalytic H_2 evolution activities of S-g-C_3N_4-D obtained at different contents of DMF and (b) sulfur powder during synthesis. (c) Photocatalytic H_2 evolution activities of g-C_3N_4, g-C_3N_4-D and S-g-C_3N_4-D. (d) Photocatalytic H_2 evolution rate of S-g-C_3N_4-D at different wavelengths and (e) the corresponding AQY. (f) Photocatalytic H_2 evolution reusability of S-g-C_3N_4-D.

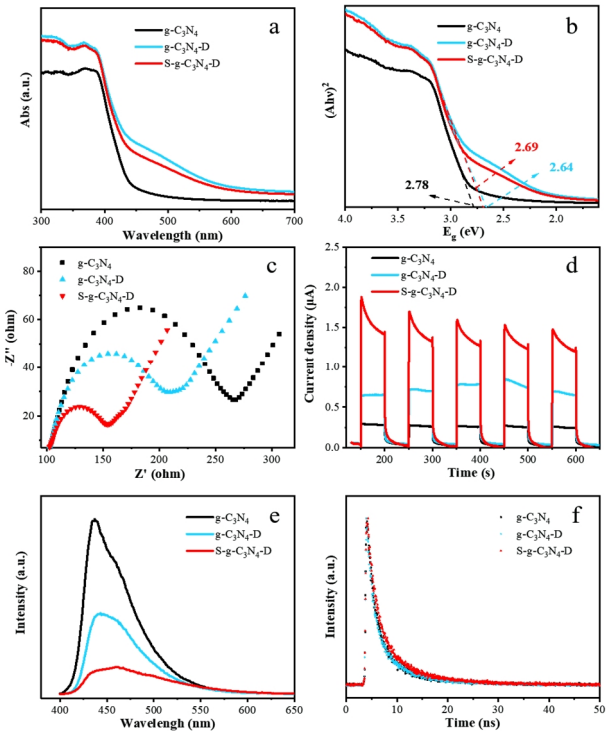

Figure 4. (a) UV-vis absorption spectra and (b) the corresponding estimated energy gaps of g-C_3N_4, g-C_3N_4-D and S-g-C_3N_4-D. (c) EIS plots and (d) transient photocurrent responses of g-C_3N_4, g-C_3N_4-D and S-g-C_3N_4-D. (e) Photoluminescence spectra and (f) the corresponding transient fluorescence decay spectra of g-C_3N_4, g-C_3N_4-D and S-g-C_3N_4-D.

suitable additive contents of powdered sulfur are found to be 20 mL and 4 g, respectively. Therefore, the photocatalysts discussed below are synthesized under the conditions of above-mentioned optimal additive amounts. Figure 3c presents the photocatalytic activities of g-C_3N_4, g-C_3N_4-D and S-g-C_3N_4-D for H_2 evolution. Expectedly, the pristine g-C_3N_4 exhibits a relatively poor photocatalytic H_2 evolution rate of 373.6 μmol·h^{-1}·g^{-1}, while the significantly improved photocatalytic H_2-generation efficiency is obtained over the g-C_3N_4-D sample, indicating the introduction of abundant defects into g-C_3N_4 framework effectively promotes the photocatalytic reduction process of hydrogen ions. Particularly, the S-g-C_3N_4-D catalyst possesses the highest photocatalytic activity with a H_2 evolution rate of 3110.1 μmol h^{-1}·g^{-1}, which is 1.89 and 8.33 times higher than that of g-C_3N_4-D (1650.3 μmol·h^{-1}·g^{-1}) and g-C_3N_4 (373.6 μmol·h^{-1}·g^{-1}), strongly confirming the important role of S-doping and defects in improving the photocatalytic activity of H_2 evolution. Figure 3d and 3e displays the photocatalytic H_2 evolution rate and apparent quantum efficiencies (AQE) of S-g-C_3N_4-D under different wavelengths, in which the AQE values of 6.7%, 1.6% and 0.3% at λ = 365 nm, λ = 420 nm and λ = 500 nm, further indicating the outstanding photocatalytic H_2 evolution activity of S-g-C_3N_4-D photocatalyst. As a result, the explored S-g-C_3N_4-D material demonstrates one of the best photocatalytic H_2 evolution performances among the other S-doped C_3N_4 relevant photocatalysts reported recently (Table S3). In addition to displaying outstanding photocatalytic H_2 evolution activity, the cycling stability is another important parameter that must be considered in practical applications of an ideal photocatalyst. Thus, the durability of S-g-C_3N_4-D sample is also evaluated by comparing the attenuation of photocatalytic H_2 evolution before and after six consecutive cycles (Figure 3f). Remarkably, the S-g-C_3N_4-D exhibits the negligible variation of photocatalytic performance after prolonged visible light irradiation for 24 h, convincingly suggesting the robust stability and excellent availability of developed S-g-C_3N_4-D. Particularly, a small increased amount of H_2 evolution is observed after 4th cycle, which can be attributed to the exposure of more photocatalytic active sites over the developed S-g-C_3N_4-D sample, thereby accelerating the H_2 evolution activity.[55]

In order to explore the reasons for the outstanding photocatalytic H_2 evolution activity of S-g-C_3N_4-D incisively, the light absorption capacity and band gap energy (E_g) of obtained photocatalysts, as well the separation, transfer and recombination efficiency of photo-excited electron-hole pairs are investigated systematically. Figure 4a and 4b display the UV-vis diffuse reflection spectra and the corresponding estimated energy gaps of g-C_3N_4, g-C_3N_4-D and S-g-C_3N_4-D. Obviously, the g-C_3N_4-D and S-g-C_3N_4-D catalysts possess the wider light response range with higher absorption strength in comparison to those of g-C_3N_4, which indicates that the integration of S-doping and defects are significantly beneficial to the enhancement of the absorption of photons. Notably, the absorption boundary of S-g-C_3N_4-D exhibits a slight blue shift compared with that of g-C_3N_4-D, which results from the quantum confinement effect caused by S-doping.

DOI: 10.14102/j.cnki.0254-5861.2021-0039

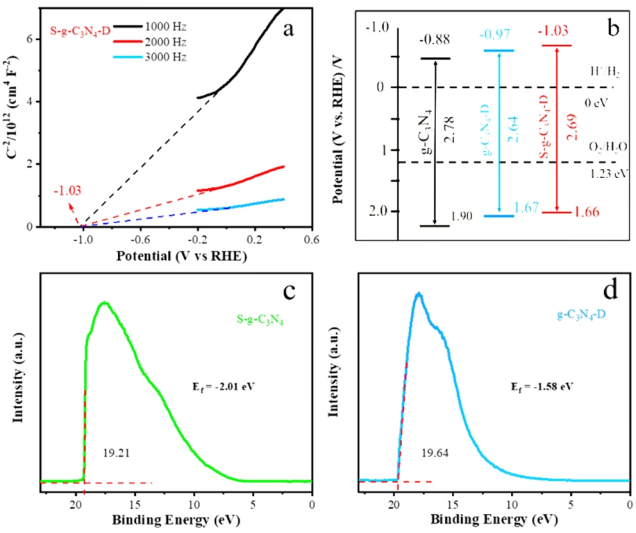

Figure 5. (a) Mott-Schottky plots of S-g-C_3N_4-D obtained from different frequencies. (b) The band structure alignments of g-C_3N_4, g-C_3N_4-D and S-g-C_3N_4-D. (c) The UPS spectra of S-g-C_3N_4 and (d) g-C_3N_4-D.

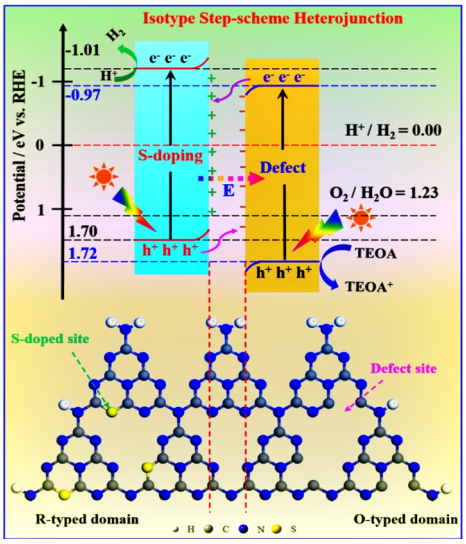

Figure 6. The band edge bending, internal electric field, charge transfer mechanism and structural configuration of sulfur-doped g-C_3N_4/defective g-C_3N_4 isotype step-scheme heterojunction.

To disclose the changes in band structure of g-C_3N_4 after S-doping and introducing defects, the E_g energies of g-C_3N_4, g-C_3N_4-D and S-g-C_3N_4-D are acquired according to the Kubelk-Munk method. As displayed in Figure 4b, the estimated band gaps of S-g-C_3N_4-D is found to be 2.69 eV, which is much narrower than that of g-C_3N_4 (2.78 eV), suggesting the rapid transition of photo-generated charges and holes over the S-g-C_3N_4-D. Figure 4c and 4d present the electrochemical impedance spectra (EIS) and transient photocurrent responses of developed catalysts, in which the strongest photocurrent densities with the smallest Nyquist plots semicircle indicate the most efficient separation efficiency and the lowest charge transfer resistance of S-g-C_3N_4-D compared with those of g-C_3N_4 and g-C_3N_4-D. Such a result convincingly confirms that the integration of defects and S-dopants effectively boost the interfacial charge separation and transfer of g-C_3N_4, thereby enhancing the photocatalytic H_2-generation performance. The recombination and lifetime of photo-excited charge carriers are uncovered by photoluminescence (PL) techniques. The steady-state PL emission spectra displayed in Figure 4e reveal that the pristine g-C_3N_4 exhibits an intense emission peak at around 450 nm, which results from the sudden recombination of charge carriers. As a sharp contrast, the distinctly feeble intensity of PL emission of g-C_3N_4-D suggests the dramatically suppressed recombination of electron-hole pairs, which mainly ascribes to the delocalization of valence electron, enhances the electronic transitions, resulting from the introduction of abundant defects. Impressively, the PL intensity is further reduced after the integration of S-dopants as observed in Figure 4e, which attributes to the trapping effect of photo-excited electrons by the S-doped sites, consequently inhibiting the recombination of charged carriers. Moreover, the S-g-C_3N_4-D catalyst possesses a wider photovoltaic response wavelength range, indicating the most efficient light absorption capacity, which agrees well with the results of UV-vis absorption spectra (Figure 4a). In addition, the transient fluorescence decays are recorded at the corresponding emission peaks to study the survival times (τ) of photo-generated charge carriers. As presented in Figure 4f and Table S4, the average carrier lifetime (τ_{Avg}) of S-g-C_3N_4-D catalyst is calculated to be 5.215 ns, which is much longer than that of g-C_3N_4 (4.190 ns), suggesting a significant positive effect of S-doping and induced defects in extending the survival time of photo-excited carriers. According to the above discussions, the integration of S dopants and defects can not only enhance the transfer and separation efficiency, but also improve the lifetime of photo-generated electron-hole pairs, thus resulting in the efficient photocatalytic H_2 evolution performance.

The possible mechanism of the catalytic H_2 evolution process of S-doped defect-rich g-C_3N_4 photocatalyst is proposed from the perspective of structural configuration and energy band theory. The conduction bands (CB) of g-C_3N_4, g-C_3N_4-D and S-g-C_3N_4-D catalysts are initially measured by the corresponding Mott-Schottky plots at different frequencies, as exhibited in Figure 5a and S7. After potential conversion, the CB potentials of g-C_3N_4, g-C_3N_4-D and S-g-C_3N_4-D are calculated to be –0.88, –0.97 and –1.03 V vs. RHE. In addition, combined with the bandgap energy mentioned above, the corresponding valence band (VB) positions are established respectively as 1.90 V of g-C_3N_4, 1.67 V of g-C_3N_4-D, and 1.66 V of S-g-C_3N_4-D. The band structure alignments with respect to RHE are described in Figure 5b, of which the band gap between CB and VB all encompasses the energy levels of water oxidation and reduction, indicating the feasibility of H_2 evolution. Additionally, the CB position of S-g-C_3N_4-D migrates respectively by 0.15 and 0.06 eV in the negative direction relative to that of g-C_3N_4 and g-C_3N_4-D, which reveals the enhanced reduction properties of photo-generated electron for S-g-C_3N_4-D sample, thereby facilitating the photocatalytic H_2 generation. Furthermore, the positive curvilinear incline slopes presented in Figure S7b and S8c suggest that both the S-doped and defective active sites display the typical N-type semiconductor characteristic. In addition, the ultraviolet photoelectron spectroscopy (UPS) of S-g-C_3N_4 and g-C_3N_4-D is recorded at the excitation energy of 21.22 eV (He Ⅰ) vs. the vacuum level (Vac) to accurately evaluate the definite direction of electron transfer between the sulfur-doped and defective active sites. Figure 5c

DOI: 10.14102/j.cnki.0254-5861.2021-0039

and 5d displays the UPS results of S-g-C_3N_4 and g-C_3N_4-D. The corresponding work function can be calculated by subtracting the electron cutoff energy, which stands for the difference between the vacuum level (0 eV) and Fermi level (E_f). Accordingly, the E_f values of S-g-C_3N_4 and g-C_3N_4-D are found to be –2.01 and –1.58 eV, respectively. Therefore, the electron will migrate from the defective active positions to the sulfur-doped active sites, which is the same electron transfer mechanism as the step-scheme heterojunction.

On the basis of the above analysis, the noteworthy N-type semiconductor characteristic accompanied by the high-and-low CB and VB positions, as well as the distinct direction of electron transfer indicates the establishment of a memorable isotype step-scheme heterojunction between the sulfur-doped and defective active sites in the structural configuration of the S-g-C_3N_4-D photocatalyst. As displayed in Figure 6, the S-doped active sites in the microstructural unit of S-g-C_3N_4-D exhibit the higher CB and VB position, corresponding to the reduction-typed domains, while the defect sites are assigned to the oxidation-typed domains with the lower CB and VB position.[35,56–58] Therein, the electrons in S-doped position spontaneously transfer to defective sites across the close contact between the two active sites, resulting in the positively charged S-doping domain and negatively charged defect domain.[28,59] Spontaneously, an internal electric field (E) is constructed at the interface, which further endows the bending of band edge (Figure 6). Therefore, the unserviceable electrons on the CB of defect location and the unnecessary holes on the VB of S-doping position recombine each other under the drive of coulomb interaction, internal electric field band edge bending in the process of photocatalytic H_2 evolution.[60,61] Meanwhile, the valuable electrons with strong reducibility and stronger oxidability of holes are enriched in the CB of S-doping and the VB of defect sites, which devotes to the supreme redox capacity of S-g-C_3N_4-D photocatalyst,[62,63] thereby endowing the strong driving force for photocatalytic H_2 evolution.

n CONCLUSION

In summary, a neoteric metal-free isotype step-scheme heterojunction composed by sulfur-dopants and abundant defects (S-g-C_3N_4-D) has been successfully developed *via* in-situ pyrolysis of DMF, urea and powdered sulfur. The resulting catalyst not only displays well-defined lamellar morphology with large surface areas, but also possesses good fluffiness and dispersibility due to the federative integration of S-dopants and defects. Therein, the high-temperature polymerization between the amide group of urea molecule and the amino groups of DMF plays an indelible role in the formation of abundant defects. Attributed to the advantageous characteristics of defect-rich lamellar nanoskeleton, sulfur-doped micr/mesoporous nanoframework, and excellent photoelectrochemical properties, as well as the construction of sulfur-doped g-C_3N_4/defective g-C_3N_4 isotype step-scheme heterojunction, the photocatalytic H_2 evolution rate of S-g-C_3N_4-D is almost 9 times higher than that of pristine g-C_3N_4. Most importantly, this work will offer some new insights for the fabrication of g-C_3N_4-based metal-free isotype step-scheme heterojunction. Additionally, the developed in-situ synthesis strategy in this work will provide some accomplished methodologies for synthesizing other multifunctional nanomaterials, including photocatalysts and electrocatalysts.

n EXPERIMENTAL

Preparation of Graphitic-carbon Nitride (g-C_3N_4). 15 g of urea was annealed at 400 °C for 1 h and calcined at 550 °C for another 3 h with a ramp rate of 15 ℃ under air atmosphere to from a yellow-colored graphitic-carbon nitride (g-C_3N_4).

Fabrication of Sulfur-doped Defect-rich Graphitic-carbon Nitride (S-g-C_3N_4-D). Typically, 15 g of urea and 4 g of powdered sulfur were added into 20 mL of N,N-dimethylformamide (DMF) under continuous stirring at 25 ℃ for 0.5 h to form a uniform yellow liquid mixture. Sebsequently, the yellow mixture was directly annealed at 400 °C for 1 h and calcined at 550 °C for another 3 h with a ramp rate of 15 ℃ under air atmosphere. After natural cooling, the sulfur-doped defect-rich graphitic-carbon nitride photocatalyst was obtained and designated as S-g-C_3N_4-D. For comparison, the defect-rich graphitic-carbon nitride (g-C_3N_4-D) sample was prepared in a similar way without the addition of powdered sulfur. Moreover, the S-g-C_3N_4-D photocatalysts obtained at different contents of DMF and powdered sulfur were also synthesized to optimize photocatalytic performance.

Photocatalytic Hydrogen Evolution Tests. The photocatalytic hydrogen evolution measurements were carried out in a full glass automatic on-line four trace gas analysis system (Labsolar-6A, Beijing PerfectLight, China). A Xe lamp with an output power of 300 W (with a $\lambda \geq 420$ nm cutoff filter as simulated visible light) acted as the light source. In a typical process, 10 mL of triethanolamine (TEOA, sacrificial electron donors) and 20 mg of as-prepared photocatalysts were added into 90 mL of deionized water. Then, 3 wt% of platinum provided by $H_2PtCl_6 \cdot 6H_2O$ was added to the mixed solution as a co-catalyst. Necessarily, the above photocatalyst solution was sonicated for at least 30 min before light exposure. Moreover, the photoreactor was also evacuated for 10 min until the air was completely removed before testing. During photocatalytic tests, the suspension was stirred continually, and the gas concentration balance was flowed by a fan. Additionally, the circulating cooling water (10 ℃) system was kept open throughout the whole photocatalytic H_2 reaction process to eliminate the thermal effect of photocatalysts. The generated H_2 by photocatalytic reaction was detected by an online gas chromatograph accompanied by a thermal conductivity detector (GC9790Ⅱ, China) with Argon as carrier gas. The amount of generated H_2 was estimated from the corresponding calibration plot. The apparent quantum efficiency (AQE) of S-g-C_3N_4-D was measured according to the following equations.

$$\mathrm{AQE}(\%) = \frac{number\ of\ reacted\ electrons}{number\ of\ incident\ photons} \times 100\%$$

$$= \frac{2 \times number\ of\ evolved\ H_2\ molecules}{number\ of\ incident\ photons} \times 100\%$$

n ACKNOWLEDGEMENTS

This work was supported by the National Natural Science Foundation of China (No. 62004143), the Central Government Guided Local Science and Technology Development Special Fund Project (No. 2020ZYYD033), the Natural Science Founda-

DOI: 10.14102/j.cnki.0254-5861.2021-0039

tion of Hubei Province (No. 2021CFB133), the Opening Fund of Key Laboratory of Rare Mineral Ministry of Natural Resources (No. KLRM-KF 202005), the Open Research Fund of Key Laboratory of Material Chemistry for Energy Conversion and Storage (HUST), Ministry of Education (No. 2021JYBKF05), the Opening Fund of Key Laboratory for Green Chemical Process of Ministry of Education of Wuhan Institute of Technology (No. GCP202101) and the Innovation Project of Engineering Research Center of Phosphorus Resources Development and Utilization of Ministry of Education (No. LCX2021003). This work is dedicated to celebrating the 50th anniversary of Wuhan Institute of Technology.

n AUTHOR CONTRIBUTIONS

H.W., J.J., J.Z. designed the proposal and wrote the manuscript. All authors have given approval to the final version of the manuscript.

n AUTHOR INFORMATION

Corresponding authors. Email: 027wit@163.com (J. Jiang), wanghaitao@wit.edu.cn (H. Wang), xinli@scau.edu.cn (X. Li)

n COMPETING INTERESTS

The authors declare no competing interests.

n ADDITIONAL INFORMATION

Supplementary information is available for this paper at http://manu30.magtech.com.cn/jghx/EN/10.14102/j.cnki.0254-5861.2021-0039

For submission: https://mc03.manuscriptcentral.com/cjsc

n REFERENCES

(1) Liao, G. F.; Gong, Y.; Zhang, L.; Gao, H. Y.; Yang, G. J.; Fang, B. Z. Semiconductor polymeric graphitic carbon nitride photocatalysts: the “holy grail” for the photocatalytic hydrogen evolution reaction under visible light. *Energ. Environ. Sci.* **2019**, 12, 2080–2147.

(2) Liang, Z. Z.; Shen, R. C.; Ng, Y. H.; Zhang, P.; Xiang, Q. J.; Li, X. A review on 2D MoS_2 cocatalysts in photocatalytic H_2 production. *J. Mater. Sci. Technol.* **2020**, 56, 89–121.

(3) Nasir, J. A.; Munir, A.; Ahmad, N.; ul Haq, T.; Khan, Z.; Rehman, Z. Photocatalytic Z-scheme overall water splitting: recent advances in theory and experiments. *Adv. Mater.* **2021**, 2105195.

(4) He, K. L.; Xie, J.; Liu, Z. Q.; Li, N.; Chen, X. B.; Hu, J.; Li, X. Multifunctional Ni_3C cocatalyst/g-C_3N_4 nanoheterojunctions for robust photocatalytic H_2 evolution under visible light. *J. Mater. Chem. A* **2018**, 6, 13110–13122.

(5) Wang, Z.; Li, C.; Domen, K. Recent developments in heterogeneous photocatalysts for solar-driven overall water splitting. *Chem. Soc. Rev.* **2019**, 48, 2109–2125.

(6) Ganguly, P.; Harb, M.; Cao, Z.; Cavallo, L.; Breen, A.; Dervin, S.; Dionysiou, D. D.; Pillai, S. C. 2D nanomaterials for photocatalytic hydrogen production. *ACS Energy Lett.* **2019**, 4, 1687–1709.

(7) Ai, L.; Shi, R.; Yang, J.; Zhang, K.; Zhang, T. R.; Lu, S. Y. Efficient combination of g-C_3N_4 and CDs for enhanced photocatalytic performance: a review of synthesis, strategies, and applications. *Small* **2021**, 2007523.

(8) Fujishima, A.; Honda, K. Electrochemical photolysis of water at a semiconductor electrode. *Nature* **1972**, 238, 37.

(9) Xing, W. N.; Tu, W. G.; Ou, M.; Wu, S. Y.; Yin, S. M.; Wang, H. J.; Chen, G.; Xu, R. Anchoring active Pt^{2+}/Pt^0 hybrid nanodots on g-C_3N_4 nitrogen vacancies for photocatalytic H_2 evolution. *ChemSusChem* **2019**, 12, 2029–2034.

(10) Liu, J.; Liu, Y.; Liu, N. Y.; Han, Y. Z.; Zhang, X.; Huang, H.; Lifshitz, Y.; Lee, S. T.; Zhong, J.; Kang, Z. H. Metal-free efficient photocatalyst for stable visible water splitting via a two-electron pathway. *Science* **2015**, 347, 970–974.

(11) Jiang, H.; Xing, Z.; Zhao, T.; Yang, Z.; Wang, K.; Li, Z.; Yang, S.; Xie, L.; Zhou, W. Plasmon Ag nanoparticle/Bi_2S_3 ultrathin nanobelt/oxygen-doped flower-like MoS_2 nanosphere ternary heterojunctions for promoting charge separation and enhancing solar-driven photothermal and photocatalytic performances. *Appl. Catal., B: Environ.* **2020**, 274, 118947.

(12) Hisatomi, T.; Kubota, J.; Domen, K. Recent advances in semiconductors for photocatalytic and photoelectrochemical water splitting. *Chem. Soc. Rev.* **2014**, 43, 7520–7535.

(13) Jiang, J.; Ou-yang, L.; Zhu, L.; Zheng, A.; Zou, J.; Yi, X.; Tang, H. Dependence of electronic structure of g-C_3N_4 on the layer number of its nanosheets: a study by Raman spectroscopy coupled with first-principles calculations. *Carbon* **2014**, 80, 213–221.

(14) Xia, P.; Cheng, B.; Jiang, J.; Tang, H. Localized π-conjugated structure and EPR investigation of g-C_3N_4 photocatalyst. *Appl. Surf. Sci.* **2019**, 487, 335–342.

(15) Jiang, J.; Li, N.; Zou, J.; Zhou, X.; Eda, G.; Zhang, Q.; Zhang, H.; Li, L. J.; Zhai, T.; Wee, A. T. S. Synergistic additive-mediated CVD growth and chemical modification of 2D materials. *Chem. Soc. Rev.* **2019**, 48, 4639–4654.

(16) Xu, C. Q.; Zhang, W. D.; Deguchi, K.; Ohki, S.; Shimizu, T.; Ma, R.; Sasaki, T. Construction of a push-pull system in g-C_3N_4 for efficient photocatalytic hydrogen evolution under visible light. *J. Mater. Chem. A* **2020**, 8, 13299–13310.

(17) Xia, P.; Cao, S.; Zhu, B.; Liu, M.; Shi, M.; Yu, J.; Zhang, Y. Designing a 0D/2D S-scheme heterojunction over polymeric carbon nitride for visible-light photocatalytic inactivation of bacteria. *Angew. Chem. Int. Ed.* **2020**, 59, 5218–5225.

(18) Wang, Y.; Liu, L.; Ma, T.; Zhang, Y.; Huang, H. 2D graphitic carbon nitride for energy conversion and storage. *Adv. Funct. Mater.* **2021**, 31, 2102540.

(19) Tu, W.; Xu, Y.; Wang, J.; Zhang, B.; Zou, T.; Yin, S.; Wu, S.; Li, C.; Huang, Y.; Zhou, Y.; Robertson, J.; Kraft, M.; Xu, R. Investigating the role of tunable nitrogen vacancies in graphitic carbon nitride nanosheets for efficient visible-light-driven H_2 evolution and CO_2 reduction. *ACS Sustain. Chem. Eng.* **2017**, 5, 7260–7268.

(20) Che, W.; Cheng, W.; Yao, T.; Tang, F.; Liu, W.; Su, H.; Huang, Y.; Liu, Q.; Liu, J.; Hu, F.; Pan, Z.; Sun, Z.; Wei, S. Fast photoelectron transfer in (C_{ring})-C_3N_4 plane heterostructural nanosheets for overall water splitting. *J. Am. Chem. Soc.* **2017**, 139, 3021–3026.

(21) Luo, J.; Wang, M.; Chen, L.; Shi, J. Efficient benzaldehyde photosynthesis coupling photocatalytic hydrogen evolution. *J. Energy Chem.* **2022**, 66, 52–60.

(22) Liang, J.;Yang, X.; Wang, Y.; He, P.; Fu, H.; Zhao, Y.; Zou, Q.; An, X. A review on g-C_3N_4 incorporated with organics for enhanced photocatalytic water splitting. *J. Mater. Chem. A* **2021**, 9, 12898–12922.

(23) Yang, W.; Ma, G.; Fu, Y.; Peng, K.; Yang, H.; Zhan, X.; Yang, W.; Wang, L.; Hou, H. Rationally designed Ti_3C_2 MXene@TiO_2/$CuInS_2$ Schottky/S-scheme integrated heterojunction for enhanced photocatalytic hydrogen evolution. *Chem. Eng. J.* **2022**, 429, 132381.

(24) Yan, J.; Wang, T.; Qiu, S.; Song, Z.; Zhu, W.; Liu, X.; Lian, J.; Sun, C.; Li, H. Insights into the efficient charge separation over Nb_2O_5/2D-C_3N_4 heterostructure for exceptional visible-light driven H_2 evolution. *J. Energy Chem.* **2022**, 65, 548–555.

DOI: 10.14102/j.cnki.0254-5861.2021-0039

(25) Xi, Y.; Chen, W.; Dong, W.; Fan, Z.; Wang, K.; Shen, Y.; Tu, G.; Zhong, S.; Bai, S. Engineering an interfacial facet of S-scheme heterojunction for improved photocatalytic hydrogen evolution by modulating the internal electric field. *ACS Appl. Mater. Interfaces* **2021**, 13, 39491–39500.

(26) Gogoi, D.; Shah, A. K.; Rambabu, P.; Qureshi, M.; Golder, A. K.; Peela, N. R. Step-scheme heterojunction between CdS nanowires and facet-selective assembly of MnO_x-$BiVO_4$ for an efficient visible-light-driven overall water splitting. *ACS Appl. Mater. Interfaces* **2021**, 13, 45475–45487.

(27) Zou, J.; Deng, W.; Jiang, J.; Arramel; He, X.; Li, N.; Fang, J.; Hsu, J. P. Built-in electric field-assisted step-scheme heterojunction of carbon nitride-copper oxide for highly selective electrochemical detection of p-nonylphenol. *Electrochim. Acta* **2020**, 354, 136658.

(28) Li, Y. F.; Zhou, M. H.; Cheng, B.; Shao, Y. Recent advances in g-C_3N_4-based heterojunction photocatalysts. *J. Mater. Sci. Technol.* **2020**, 56, 1–17.

(29) Wageh, S.; Al-Ghamdi, A. A.; Jafer, R.; Li, X.; Zhang, P. A new heterojunction in photocatalysis: S-scheme heterojunction. *Chin. J. Catal.* **2021**, 42, 667–669.

(30) Xu, Q.; Zhang, L.; Cheng, B.; Fan, J.; Yu, J. S-scheme heterojunction photocatalyst. *Chem* **2020**, 6, 1543–1559.

(31) Wang, Y.; Hao, X.; Zhang, L.; Jin, Z.; Zhao, T. Amorphous Co_3S_4 nanoparticle-modified tubular g-C_3N_4 forms step-scheme heterojunctions for photocatalytic hydrogen production. *Catal. Sci. Technol.* **2021**, 11, 943–955.

(32) Li, X.; Zhang, J.; Huo, Y.; Dai, K.; Li, S.; Chen, S. Two-dimensional sulfur- and chlorine-codoped g-C_3N_4/CdSe-amine heterostructures nanocomposite with effective interfacial charge transfer and mechanism insight. *Appl. Catal. B: Environ.* **2021**, 280, 119452.

(33) Chen, Y.; Su, F.; Xie, H.; Wang, R.; Ding, C.; Huang, J.; Xu, Y.; Ye, L. One-step construction of S-scheme heterojunctions of N-doped MoS_2 and S-doped g-C_3N_4 for enhanced photocatalytic hydrogen evolution. *Chem. Eng. J.* **2021**, 404, 126498.

(34) Huang, Y.; Mei, F. F.; Zhang, J. F.; Dai, K.; Dawson, G. Construction of 1D/2D $W_{18}O_{49}$/porous g-C_3N_4 S-scheme heterojunction with enhanced photocatalytic H_2 evolution. *Acta Phys.-Chim. Sin.* **2022**, 38, 2108028.

(35) Fu, J.; Xu, Q.; Low, J.; Jiang, C.; Yu, J. Ultrathin 2D/2D WO_3/g-C_3N_4 step-scheme H_2-production photocatalyst. *Appl. Catal., B: Environ.* **2019**, 243, 556–565.

(36) Li, B.; Zhang, B.; Zhang, Y.; Zhang, M.; Huang, W.; Yu, C.; Sun, J.; Feng, J.; Dong, S.; Sun, J. Porous g-C_3N_4/TiO_2 S-scheme heterojunction photocatalyst for visible-light driven H_2 production and simultaneous wastewater purification. *Int. J. Hydrogen Energy* **2021**, 46, 32413–32424.

(37) Qin, D.; Xia, Y.; Li, Q.; Yang, C.; Qin, Y.; Lv, K. One-pot calcination synthesis of $Cd_{0.5}Zn_{0.5}S$/g-C_3N_4 photocatalyst with a step-scheme heterojunction structure. *J. Mater. Sci. Technol.* **2020**, 56, 206–215.

(38) Song, T.; Xie, C.; Matras-Postolek, K.; Yang, P. 2D Layered g-C_3N_4/WO_3/WS_2 S-scheme heterojunctions with enhanced photochemical performance. *J. Phys. Chem. C* **2021**, 125, 19382–19393.

(39) Huang, Y.; Liu, J.; Zhao, C.; Jia, X.; Ma, M.; Qian, Y.; Yang, C.; Liu, K.; Tan, F.; Wang, Z.; Li, X.; Qu, S.; Wang, Z. Facile synthesis of defect-modified thin-layered and porous g-C_3N_4 with synergetic improvement for photocatalytic H_2 production. *ACS Appl. Mater. Interfaces* **2020**, 12, 52603–52614.

(40) Cui, M.; Cui, K.; Liu, X.; Chen, X.; Chen, Y.; Guo, Z. Roles of alkali metal dopants and surface defects on polymeric carbon nitride in photocatalytic peroxymonosulfate activation towards water decontamination. *J. Hazard. Mater.* **2022**, 424, 127292.

(41) Yu, G.; Zhao, H.; Xing, C.; Guo, L.; Li, X. Creation of carbon defects and in-plane holes with the assistance of NH_4Br to enhance the photocatalytic activity of g-C_3N_4. *Catal. Sci. Technol.* **2021**, 11, 5349–5359.

(42) Li, X.; Kang, B.; Dong, F.; Zhang, Z.; Luo, X.; Han, L.; Huang, J.; Feng, Z.; Chen, Z.; Xu, J.; Peng, B.; Wang, Z. Enhanced photocatalytic degradation and H_2/H_2O_2 production performance of S-pCN/$WO_{2.72}$ S-scheme heterojunction with appropriate surface oxygen vacancies. *Nano Energy* **2021**, 81, 105671.

(43) Chen, L.; Zhu, D.; Li, J.; Wang, X.; Zhu, J.; Francis, P. S.; Zheng, Y. Sulfur and potassium co-doped graphitic carbon nitride for highly enhanced photocatalytic hydrogen evolution. *Appl. Catal., B: Environ.* **2020**, 273, 119050.

(44) Liu, Z.; Zhang, X.; Jiang, Z.; Chen, H. S.; Yang, P. Phosphorus and sulphur co-doping of g-C_3N_4 nanotubes with tunable architectures for superior photocatalytic H_2 evolution. *Int. J. Hydrogen Energy* **2019**, 44, 20042–20055.

(45) Lv, H.; Huang, Y.; Koodali, R. T.; Liu, G.; Zeng, Y.; Meng, Q.; Yuan, M. Synthesis of sulfur-doped 2D graphitic carbon nitride nanosheets for efficient photocatalytic degradation of phenol and hydrogen evolution. *ACS Appl. Mater. Interfaces* **2020**, 12, 12656–12667.

(46) Wang, H.; Bian, Y.; Hu, J.; Dai, L. Highly crystalline sulfur-doped carbon nitride as photocatalyst for efficient visible-light hydrogen generation. *Appl. Catal., B: Environ.* **2018**, 238, 592–598.

(47) Wang, H.; Qiu, X.; Peng, Z.; Wang, W.; Wang, J.; Zhang, T.; Jiang, L.; Liu, H. Cobalt-gluconate-derived high-density cobalt sulfides nanocrystals encapsulated within nitrogen and sulfur dual-doped micro/mesoporous carbon spheres for efficient electrocatalysis of oxygen reduction. *J. Colloid Interface Sci.* **2020**, 561, 829–837.

(48) Liu, R.; Tan, K.; Gong, Y.; Chen, Y.; Li, Z.; Xie, S.; He, T.; Lu, Z.; Yang, H.; Jiang, D. Covalent organic frameworks: an ideal platform for designing ordered materials and advanced applications. *Chem. Soc. Rev.* **2021**, 50, 120–242.

(49) Zou, J.; Wu, S.; Liu, Y.; Sun, Y.; Cao, Y.; Hsu, J. P.; Shen Wee, A. T.; Jiang, J. An ultra-sensitive electrochemical sensor based on 2D g-C_3N_4/CuO nanocomposites for dopamine detection. *Carbon* **2018**, 130, 652–663.

(50) He, X.; Bai, S.; Jiang, J.; Ong, W. J.; Peng, J.; Xiong, Z.; Liao, G.; Zou, J.; Li, N. Oxygen vacancy mediated step-scheme heterojunction of $WO_{2.9}$/g-C_3N_4 for efficient electrochemical sensing of 4-nitrophenol. *Chemical Engineering Journal Advances* **2021**, 8, 100175.

(51) Zhao, D.; Wang, Y.; Dong, C.; Huang, Y.; Chen, J.; Xue, F.; Shen, S.; Guo, L. Boron-doped nitrogen-deficient carbon nitride-based Z-scheme heterostructures for photocatalytic overall water splitting. *Nat. Energy* **2021**, 6, 388–397.

(52) Sun, Y.; Jiang, J.; Liu, Y.; Wu, S.; Zou, J. A facile one-pot preparation of Co_3O_4/g-C_3N_4 heterojunctions with excellent electrocatalytic activity for the detection of environmental phenolic hormones. *Appl. Surf. Sci.* **2018**, 430, 362–370.

(53) Zou, J.; Mao, D.; Wee, A. T. S.; Jiang, J. Micro/nano-structured ultrathin g-C_3N_4/Ag nanoparticle hybrids as efficient electrochemical biosensors for l-tyrosine. *Appl. Surf. Sci.* **2019**, 467, 608–618.

(54) Zou, J.; Mao, D.; Li, N.; Jiang, J. Reliable and selective lead-ion sensor of sulfur-doped graphitic carbon nitride nanoflakes. *Appl. Surf. Sci.* **2020**, 506, 144672.

(55) Song, H.; Liu, X.; Wang, U.; Chen, L.; Zhang, J.; Zhao, C.; He, F.; Dong, P.; Li, B.; Wang, S.; Wang, S.; Sun, H. Synergy of intermolecular donor-acceptor and ultrathin structures in crystalline carbon nitride for efficient photocatalytic hydrogen evolution. *J. Colloid Interface Sci.* **2022**, 607, 1603–1612.

(56) Li, X. B.; Liu, J. Y.; Huang, J. T.; He, C. Z.; Feng, Z. J.; Chen, Z.; Wan,

DOI: 10.14102/j.cnki.0254-5861.2021-0039

L. Y.; Deng, F. All organic S-scheme heterojunction PDI-Ala/S-C_3N_4 photocatalyst with enhanced photocatalytic performance. *Acta Phys.-Chim. Sin.* **2021**, 37, 2010030.

(57) Chen, Y.; Su, F.; Xie, H.; Wang, R.; Ding, C.; Huang, J.; Xu, Y.; Ye, L. One-step construction of S-scheme heterojunctions of N-doped MoS_2 and S-doped g-C_3N_4 for enhanced photocatalytic hydrogen evolution. *Chem. Eng. J.* **2021**, 404, 126498.

(58) He, F.; Meng, A.; Cheng, B.; Ho, W.; Yu, J. Enhanced photocatalytic H_2-production activity of WO_3/TiO_2 step-scheme heterojunction by graphene modification. *Chin. J. Catal.* **2020**, 41, 9–20.

(59) Ren, D.; Zhang, W.; Ding, Y.; Shen, R.; Jiang, Z.; Lu, X.; Li, X. In situ fabrication of robust cocatalyst-free CdS/g-C_3N_4 2D-2D step-scheme heterojunctions for highly active H_2 evolution. *Solar RRL* **2020**, 4, 1900423.

(60) Cheng, C.; He, B.; Fan, J.; Cheng, B.; Cao, S.; Yu, J. An inorganic/organic S-scheme heterojunction H_2-production photocatalyst and its charge transfer mechanism. *Adv. Mater.* **2021**, 33, 2100317.

(61) Xu, Q.; Zhang, L.; Cheng, B.; Fan, J.; Yu, J. S-scheme heterojunction photocatalyst. *Chem* **2020**, 6, 1543–1559.

(62) Xia, P.; Cao, S.; Zhu, B.; Liu, M.; Shi, M.; Yu, J.; Zhang, Y. Designing a 0D/2D S-scheme heterojunction over polymeric carbon nitride for visible-light photocatalytic inactivation of bacteria. *Angew. Chem. Int. Ed.* **2020**, 59, 5218–5225.

(63) Xu, F.; Meng, K.; Cheng, B.; Wang, S.; Xu, J.; Yu, J. Unique S-scheme heterojunctions in self-assembled TiO_2/$CsPbBr_3$ hybrids for CO_2 photoreduction. *Nat. Commun.* **2020**, 11, 4613.

Received: November 19, 2021
Accepted: December 13, 2021
Published: January 13, 2022

DOI: 10.14102/j.cnki.0254-5861.2021-0039